remote sensing

MDPI

Article

Observation of Post-Sunset Equatorial Plasma Bubbles with BDS Geostationary Satellites over South China

Guanyi Ma [1,2,*], Jinghua Li [1,2], Jiangtao Fan [1,2], Qingtao Wan [1,2], Takashi Maruyama [1,3], Liang Dong [4], Yang Gao [5,6], Le Zhang [5,6] and Dong Wang [7]

1 National Astronomical Observatories, Chinese Academy of Sciences, Beijing 100101, China; jhli@nao.cas.cn (J.L.); jtfan@nao.cas.cn (J.F.)
2 University of Chinese Academy of Sciences, Beijing 100049, China
3 National Institute of Information and Communications Technology, Koganei 184-8795, Tokyo, Japan
4 Yunnan Observatories, Chinese Academy of Sciences, Kunming 650011, China; dongliang@ynao.ac.cn
5 School of Physics and Astronomy, Sun Yat-sen University, Zhuhai 519082, China
6 CSST Science Center for the Guangdong-Hong Kong-Macau Great Bay Area, SYSU, Zhuhai 518082, China
7 Shenzhen Astronomical Observatory, Shenzhen 518121, China
* Correspondence: guanyima@nao.cas.cn

Abstract: An equatorial plasma bubble (EPB) is characterized by ionospheric irregularities which disturb radio waves by causing phase and amplitude scintillations or even signal loss. It is becoming increasingly important in space weather to assure the reliability of radio systems in both space and on the ground. This paper presents a newly established GNSS ionospheric observation network (GION) around the north equatorial ionization anomaly (EIA) crest in south China, which has a longitudinal coverage of ∼30° from 94°E to 124°E. The measurement with signals from geostationary earth orbit (GEO) satellites of the BeiDou navigation satellite system (BDS) is capable of separating the temporal and spatial variations of the ionosphere. A temporal fluctuation of TEC (TFT) parameter is proposed to characterize EPBs. The longitude of the EPBs' generation can be located with TFT variations in the time–longitude dimension. It is found that the post-sunset EPBs have a high degree of longitudinal variability. They generally show a quasiperiodic feature, indicating their association with atmospheric gravity wave activities. Wave-like structures with different scale sizes can co-exist in the same night.

Keywords: equatorial plasma bubble (EPB); temporal fluctuation of TEC (TFT); longitudinal variability; wave-like structure

Citation: Ma, G.; Li, J.; Fan, J.; Wan, Q.; Maruyama, T.; Dong, L.; Gao, Y.; Zhang, L.; Wang, D. Observation of Post-Sunset Equatorial Plasma Bubbles with BDS Geostationary Satellites over South China. *Remote Sens.* **2024**, *16*, 3521. https://doi.org/10.3390/rs16183521

Academic Editor: Yunbin Yuan

Received: 10 August 2024
Revised: 14 September 2024
Accepted: 18 September 2024
Published: 23 September 2024

1. Introduction

Equatorial plasma bubbles (EPBs) are an important issue in space weather and have continuously received great attention due to their significant effects on radio propagation, which can lead to interference in radio astronomy, ranging errors in radar, positioning errors in Global Navigation Satellite System (GNSS), and disruption of satellite or radio communication [1–7]. It is the low-density region that contains strong irregularities in the nighttime equatorial and low-latitude ionosphere. The consensus on the phenomenon and morphology of EPBs has been reached over time by radio observations with bottomside soundings, topside soundings, scintillation of radio stars, scintillation of satellite beacons, and radars; in situ measurements by satellite and rocket; optical imaging; and numerical simulations. It is well accepted that EPBs are generated as Rayleigh–Taylor (R-T) instabilities associated with the strong prereversal enhancement (PRE) of the eastward electric field after sunset at the bottomside of the F-region, and the rise to the topside ionosphere. While extending along the magnetic field away from the magnetic equator, they often reach the equatorial ionization anomaly (EIA) crest, form elongated, wedge-like structures in the east–west, and drift eastward at a speed of 100 m/s. Extensive studies have been subsequently carried out with both observational and theoretical research over the past decades

and have revealed the occurrence characteristics, evolution process, longitudinal variability, temporal variation, and solar and geomagnetic activity dependences of EPBs. However, the factors determining the day-to-day and longitudinal variation of EPB occurrence are still not clarified [8,9].

Regarding EPBs' longitudinal variability on the global scale, earlier investigations with topside sounding and in situ measurement from satellites show that in June the occurrence probability of EPBs is higher in the African than the American and Atlantic regions and in December the EPB occurrence probability is higher in the American and Atlantic regions than the other regions, which contradicts the strongest PRE of the eastward electric field in the equinoxes. Considering that the R-T growth rate is inversely proportional to the magnetic flux tube-integrated Pederson conductance from the E layer of the ionosphere, which has the largest value at the longitude where the magnetic flux tube aligns with the dusk terminator, magnetic declination is reckoned a controlling factor [10,11]. Longitudinal variation in the occurrence of EPBs on a regional scale was examined by ionosondes at two Southeast Asian sites. Separated by a distance of around 700 km, the post-sunset occurrences are often very different at the two sites. The localized prereversal enhancement of the eastward electric field is speculated to be the controlling factor, which could be a result of collisional shear instability or spatial resonance of atmospheric gravity waves [12]. The radar observations at Kototabang and Sanya (∼1000 km) also show a large difference in EPB generation rates. The significantly higher EPB generation rate over Kototabang was suggested to be linked with the more active inter-tropical convergence zone nearby, where the atmospheric gravity wave (AGW) activity could be more frequent, resulting in more intense seeding and the development of R-T instability [13]. However, these far-separated observations are not sufficient to draw generalizable conclusions. Simultaneous and successive observations with a higher longitudinal resolution should be made.

A new Global Navigation Satellite System (GNSS) ionospheric observation network (GION) at the EIA crest over China has been established by the National Astronomical Observatories of the Chinese Academy of Sciences (NAOC). Observation is carried out with signals from the BeiDou navigation satellite system (BDS) of China, the global positioning system (GPS) of the US, and the Galileo global navigation system of the European Union (GAL). Compared with onboard satellite, in situ satellite, ground-based ionosonde, radar, and optical measurements, the GNSS provides an indispensable means for regular ionospheric observation due to its passive receiving, seamless coverage, and all-weather and continuous operation. Moreover, there are seven geostationary (GEO) satellites operational over the Asia–Pacific area, as the third generation of the BDS officially started global service on 31 July 2020. The measurement with the new version of the GNSS receiver from GEO satellites is capable of separating the temporal and spatial variations of the ionosphere. This paper proposes methods to detect EPBs, to estimate their zonal speed and locate their longitude of generation with the GEO satellite of the BDS. The occurrence of EPBs can be investigated in a longitudinal width of nearly 30°. The longitude of EPBs' generation can be located. The GION observation and methodology are described in Section 2. Section 3 presents the results together with the new parameter and method to characterize EPBs. The discussion is in Section 4, and conclusions are offered in Section 5.

2. Observation and Methodology

The GION currently includes 14 GNSS receivers near the EIA crest of China, providing the carrier phase and pseudorange observables at 1 s intervals from signals of two carrier frequencies of the GNSS, which are B1 at 1568.098 MHz and B3 at 1268.52 MHz of the BDS, L1 at 1575.42 MHz and L2 at 1267.60 MHz of the GPS, and E1 at 1575.42 MHz and E5A at 1176.45 MHz of GAL. The data are transferred to the NAOC via mobile internet of things (MIoT). Figure 1 displays the map with the location of the GNSS receivers expressed in magnenta. Also shown are the ionospheric pierce points (IPPs) at 11:30 UT on 23 February 2024 by modeling the ionosphere as a thin shell of a hollow sphere co-centered with the Earth at height of 400 km. The data from the satellites with an elevation smaller than 30°

are excluded to reduce multi-path effects. The blue, green, and black dots represent the IPPs intersected by the line of sight of inclined orbit satellites from the GPS, GAL, and BDS, respectively. The red triangles represent those from the BDS GEO (BDG) satellites. The IPPs are mainly distributed in a longitude range of ∼94–124°E and a latitude range of ∼10–27°N. Most of them align longitudinally at a latitude range of 18.5–23.5°N. Benefited from a constellation with more than 50 satellites, a receiver of the GION is generally capable of receiving signals from ∼36 satellites at any time, which contributes the most. The IPPs of BDG satellites can be taken as fixed observation stations which are valuable for EPBs' study.

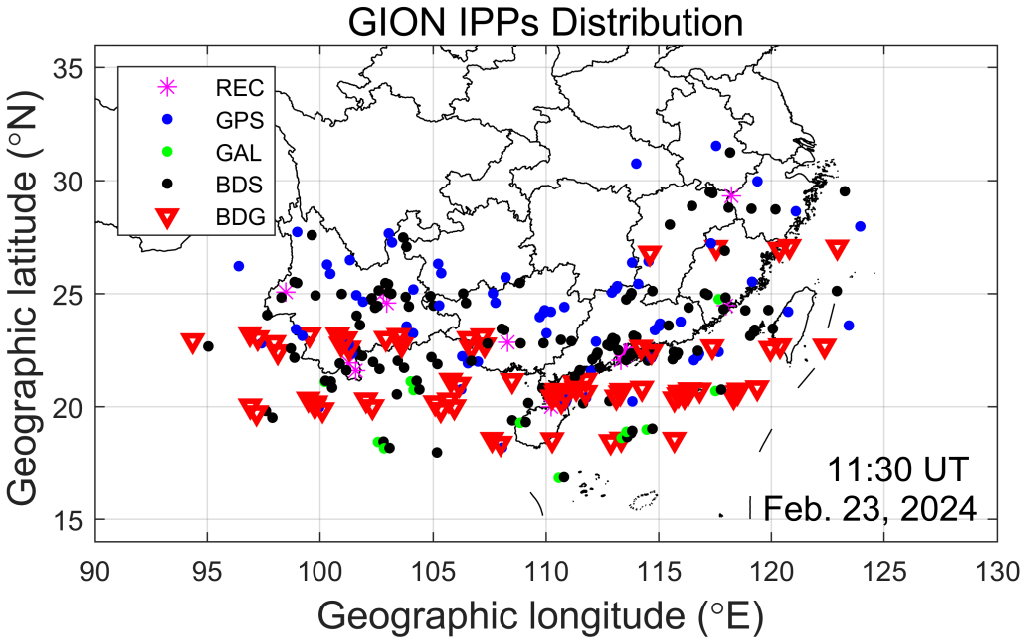

Figure 1. IPPs at a shell height of 400 km observed by the GION receivers of the BDS, GPS, and GAL at 11:30 UT on 23 February 2024. A cutoff angle of 30° is applied. The asterisk in magnenta shows the GNSS receiver's position.

The EPBs are detected and analyzed based on the ionospheric total electron content (TEC), which is proportional to the group delay and phase advance caused by the ionosphere refraction to the GNSS satellite signal. Since the carrier phase measurement has a higher precision than that of the pseudorange, we use the phase measurements to obtain slant TEC (sTEC) in 1 s intervals along the line of sight from satellite to receiver. A data screening is executed beforehand to remove possible cycle slips and discard the data with an elevation smaller than 30° [14]. The rate of TEC change (ROT) is taken from the time derivative of sTEC. The rate of the TEC index (ROTI), defined by $ROTI = \sqrt{< ROT^2 > - < ROT >^2}$, is computed with a 10 s time running window. We use the ROTI to validate the existence of EPBs, as it is often utilized to investigate the irregularity in plasma bubbles and to study the evolution of large-scale irregularities during magnetic storms at low and high latitudes [15,16]. In our observation, the ROTI generally has a mean of 0.025 TECU/s and an uncertainty of 0.025 TECU/s for no event time. We set a threshold to a ROTI > 0.2 TECU/s to identify EPBs. As the ROTI is based on the derivative of sTEC, it is not sensitive to monotonic and small-scale variations. Moreover, for most of the GNSS satellites except those of the BDG, they move very fast on an inclined orbit, from which the ROTI, labeled as ROTIi, blends the temporal and spatial variations of the ionosphere. From the BDG satellite that is stationary, the calculated ROTI is named ROTIg. It is noteworthy that ROTIg only contains the temporal variation of the ionosphere.

Furthermore, we propose a new parameter, temporal fluctuation of TEC (TFT), from a 1 Hz observation rate of BDG satellites to detect EPBs. With the single thin shell ionosphere at the height of 400 km, the vertical TEC (vTEC) at the IPP of the BDS GEO is obtained by

multiplying sTEC by the cosine of the zenith angle at the IPP. TFT is defined as the standard deviation of vTEC in a 10 s time window.

$$TFT = \sqrt{< vTEC^2 > - < vTEC >^2} \quad (1)$$

It is worth noting that TFT is a measurement of vTEC variability without system error while having the same unit as that of vTEC. The universal inter-frequency hardware bias mixed with the integer ambiguity intrinsic to vTEC is eliminated when subtracting the mean of vTEC in (1), since the IPPs of the geostationary satellites can be presumed to be stationary and the bias does not change with the times. EPBs are well manifested by depletion of and irregular variation in vTEC. TFT from BDG observation offers a new means to detect and characterize EPBs. We tag the letter g to TFT as TFTg to emphasize the fact that only a geostationary satellite is apt to provide such a measurement.

Disturbance in the ionosphere can be caused by a magnetic storm. Since storm-time EPBs would be different from quiet-time ones, the Dst index is used to check the geomagnetic condition in the process of data analysis, and it was downloaded from the GSFC/SPDF OMNIWeb interface at https://omniweb.gsfc.nasa.gov (accessed on 10 March 2024).

3. Results

Figure 2 gives an example of EPBs detected by BDG 2 at IPP (18.6°N, 108.0°E) and BDG 3 at IPP (18.7°N, 110.3°E) on 6 October 2023. The local time offset is 7.20 h and 7.35 h, respectively. On the left, the top, middle, and bottom panels show vTEC, TFTg, and ROTIg from the observation with the receiver at Hainan. Figure 2a shows vTEC variation. From left to right, three EPBs can be seen at ∼14:00–15:00 UT, ∼15:20–15:40 UT, and ∼17:25–18:10 UT, respectively. The first one has the largest TEC depletion of ∼70 TECU. The depletion of the second one is around ∼50 TECU. The third one is ∼10 TECU. Temporal fluctuation of vTEC is shown in Figure 2b. Corresponding to the EPBs, spikes of TFTg stick out. EPBs with large depletion and intense fluctuations tend to have large value of TFTg. The largest TFTg is ∼1.7 TECU, indicating the rapid variation in a 10 s time scale.

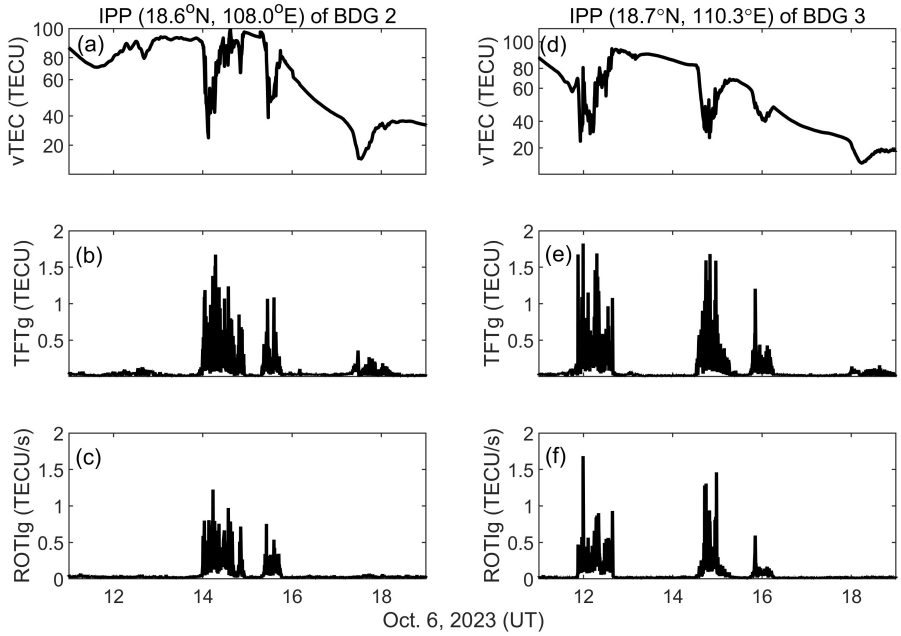

Figure 2. EPBs detected on 6 October 2023. (**a**) vTEC, (**b**) TFTg and (**c**) ROTIg in the left are from observation by BDG 2. (**d**) vTEC, (**e**) TFTg and (**f**) ROTIg in the right are from observation by BDG 3.

ROTIg in Figure 2c displays distinct spikes for the two large EPBs. It is not able to detect the small depletion and irregular variation of the third EPBs. On the right is the variation in the same parameters with time on the left. The longitude of the IPP is 110.3°E,

which is around 350 km to the east of the IPP on the left. A conspicuous vTEC depletion with strong irregularities occurred at ∼11:50 UT (19:25 LT). Then, three smaller depletions followed, appearing at ∼14:30 UT (22:05 LT), ∼15:50 UT, and ∼18:00 UT, as shown in Figure 2d. The three depletions after ∼14:30 UT resemble those in Figure 2a, although the magnitudes declined more or less. Corresponding to the four depletions, TFTg in Figure 2e shows four periods of values larger than the background. The shrink of the three previous depletions in time or magnitude can be also observed. In Figure 2f, ROTIg just shows three irregular variation structures. The later two correspond to the previous two structures shown in Figure 2c.

Note that the value of TFTg is generally 0.015 TECU. It has an uncertainty of 0.004 TECU for no EPB time. We set a threshold to TFTg $>$ 0.15 TECU to identify EPBs. ROTIg generally has a similar variation pattern to that of TFTg. However, the smallest depletion is not manifested in ROTIg, showing that ROTI is not sensitive to monotonic and small-scale variations.

Figure 3 presents the EPBs captured by the GION on 8 September 2023 in time-longitude dimensions. The morphology is manifested with TFTg from the BDG, ROTIg from the BDG, and ROTIi from the GNSS inclined satellites as shown in panels (a), (b), and (c), respectively. The plain grey in the background is for the IPPs' observation with value smaller than the threshold. The dotted lines show the sunset time at different longitudes. The EPBs spread from ∼103 to ∼120°E with three structures. The earliest EPBs are observed at ∼12:10 UT and ∼117.3°E. From both the start time boundary and the end time boundary of the structures, the longitude increases with the time, showing the eastward drift of EPBs. Since TFTg is more sensitive than the ROTI to EPBs, we can use TFTg to estimate the zonal speed of EPBs, which is ∼110 m/s. On the other hand, EPBs stick out a few minutes later successively at the ∼116.3°E area. The whole alignment is organized and forms one structure. Parallel to the first one, there are another two EPB structures that appear at (12:20 UT and 110.2°E) and (14:20 UT, 103.6°E). It can be noted that the time lag to the sunset of the third structure is a little larger than that of the other two structures. The middle panel of ROTIg and the right panel of ROTIi show almost the same pattern. The time duration and longitude width given by ROTIg and ROTIi are a little different from those shown by TFTg. All parameters clearly show quasiperiodic characteristics of the three EPB structures.

With the TFTg plot expressed in UT–longitude, the local longitude of the EPBs' source can be clearly traced back. We propose a minimum UT–longitude (mUT-Lon) method to find the generation longitude of EPBs: check the minimum UT time for all longitudes and record the corresponding longitude as the generated longitude of the first EPB structure. By repeating the minimum UT–longitude method, we can locate the longitude of the EPBs' generation for all EPB structures and count the number of EPB structures (or daily generations) for the whole longitudinal range of observation. In Figure 3, there are three generations of EPBs on 8 September 2023.

Figure 4 presents EPBs of 6 October 2023, which are distributed from ∼97 to ∼120°E. From their pattern and alignment, we can sort out three structures from left to right. For the leftmost structure, the first EPBs occur at ∼11:10 UT at 119.5°E. Continuous occurring is seen to the west in decreasing longitude with time progressing. The last noticeable one occurred at ∼11:30 UT at 110.3°E, which is shown in Figure 2d–f. Note that the outline of the structure resembles an inverted triangle. An eastward drift speed of ∼105 m/s can be estimated from the correspondence of longitude to time for the right-hand-side boundary. Inside the inverted triangle, the colored dots, at 119.5°E, for example, align continuously in time. We can speculate that the EPBs from west might catch up and merge with the ones to their east while drifting eastward. The other two EPB structures are observed to start at ∼104 and ∼97°E, respectively. They also drift eastward and have a similar speed as the first one. There are 18 generations of EPBs determined by the mUT-Lon method. The difference between any two EPBs' generation longitudes can be smaller than 1 degree. In the middle panel, Figure 4b shows three EPB structures with ROTIg, which are quite similar to Figure 4a. However, their time durations are visibly shorter than those shown

with TFTg due to the ROTI's non-sensitivity to monotonic and small-scale variations. With ROTIi in Figure 4c, three EPBs can be identified. However, it is noisier than TFTg and ROTIg somehow. The boundary of the structures is difficult to tell. Although the pattern of EPBs in Figure 4 is different from those in Figure 3, the quasiperiodic feature is undeniable.

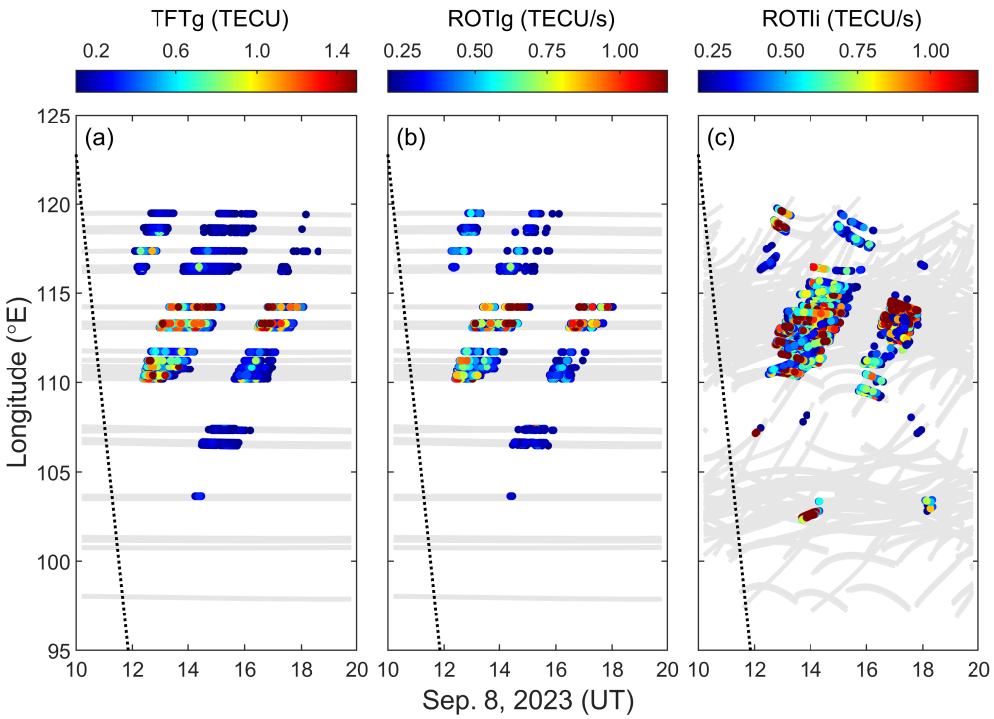

Figure 3. EPBs observed on 8 September 2023. (**a**) TFTg, (**b**) ROTIg and (**c**) ROTIi as a function of longitude and time.

Figure 5 shows EPBs' occurrence on 23 February 2024 with TFTg, ROTIg, and ROTIi. From Figure 5a, the earliest generation of EPBs is observed at 11:10 UT and 119.4°E. Then, together with the EPBs at longitudes larger than 119.4°E, an eastward drift of the EPBs can be identified since the start time boundary forms a line slanting to the right. The speed can be estimated as ∼120 m/s from the slope of the boundary. Moreover, in the following time, a series of EPBs are generated until 15:10 UT at 94.4°E. The later-generated EPBs can merge with prior ones. From the magnitude of TFTg and vague boundaries, we can discern a cluster of EPBs in the east at ∼100°E, and a few smaller structures in the west at ∼100°E, all drifting eastward. From the longitude of 103°E, the time lag of the EPBs' generation to the sunset increases with the decrease of longitude. ROTIg of Figure 5b in the middle panel shows a similar configuration in the whole range However, the cluster in Figure 5a can be seen here as two structures. To the west of ∼100°E, starting after 14 UT, the EPBs are displayed as a scatter of discrete structures rather than organized ones. The layout of ROTIi in Figure 5c is further stratified. There seem to be two or three crowded structures from ∼113°E eastward. Then, three more structures can be recognized, aligning from ∼100°E to ∼107°E. Finally, to the west of ∼100°E there are three separated structures. The EPBs in the whole observation range display a quasiperiodic pattern with a smaller scale than those in Figures 3 and 4. There are 12 EPB generations determined by the mUT-Lon method. These observation indicate that the EPBs can be generated successively in a wide longitudinal range of ∼25°.

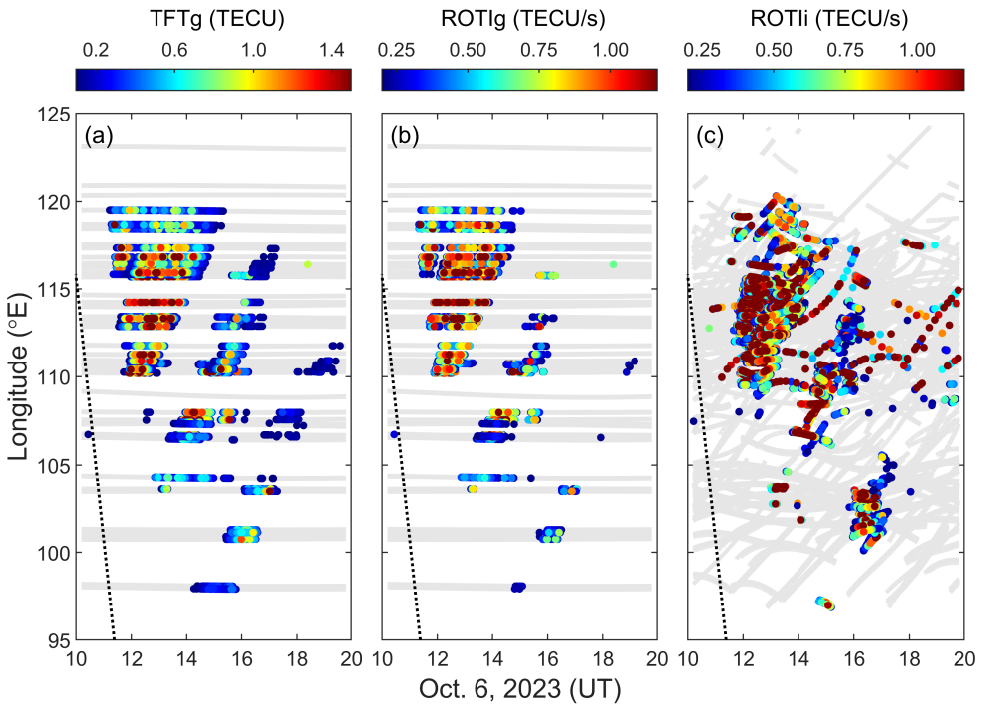

Figure 4. EPBs observed on 6 October 2023. (**a**) TFTg, (**b**) ROTIg and (**c**) ROTIi as a function of longitude and time.

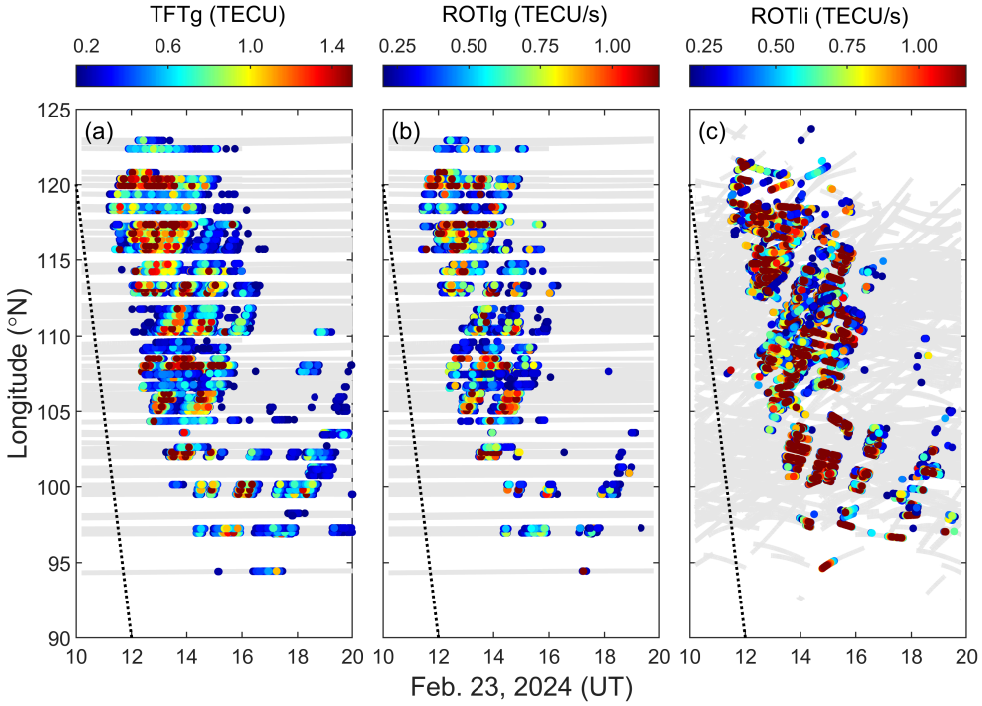

Figure 5. EPBs observed on 23 February 2024. (**a**) TFTg, (**b**) ROTIg and (**c**) ROTIi as a function of longitude and time.

The longitudinal characteristics of EPBs' occurrence and generation are very different for different days. We surveyed the data from August 2023 to February 2024. EPBs occurred intermittently from August to November of 2023. While only a few EPBs were recorded in December 2023 and January 2024, EPBs occurred almost every day in February 2024. Since the longitudinal variation is intertwined with day-to-day variability in EPB occurrence, we

select EPBs observed from August to November 2023, centering near the autumn equinox to make a statistical study.

Figure 6 presents the longitude coverage of EPBs' occurrence observed by TFTg. Most of the observation is in a longitude range, [97°E, 120°E] below a latitude of 24°N. The two EPBs observed at longitudes larger than 120°E indicate that they reached 27°N because the GNSS receiver was not set up yet in (24.5°N, 118.0°E) in October. There are 62 days with EPBs over the period of 122 days. The occurrence of EPBs generally increases with month, peaks in October, and then decreases in November. From August to November, the monthly occurrence rates are 45%, 47%, 61%, and 43%, respectively. In August and September, the longitude coverage is generally small and different in size day to day, though there are several days when EPBs are observed in a longitude range of 23°. In October, the longitude coverage is obviously large in most days. There are two days when the coverage reaches the whole observation range of 25°. In November, the longitude coverage generally becomes smaller. No regular pattern can be inferred about the longitudinal coverage of EPB occurrence in this period. The curve in red represents the Dst index of the geomagnetic activity. There is one moderate storm (-100 nT $\leq$ Dst min < -50 nT) in August. There is one moderate storm and three weak storms (-50 nT $\leq$ Dst min < -30 nT) in September. There is one moderate and one weak storm in October. In November, there are two moderate storms and one weak storm. A dip in EPB formation is noticeable with every sharp dip in Dst. This aligns with the expectation that geomagnetic activity disrupts the winds and the formation of the prereversal enhancement of the vertical plasma drift, inhibiting EPB formation. However, obvious correspondence is not perceived between both longitude coverage and daily occurrence of EPBs and the storms.

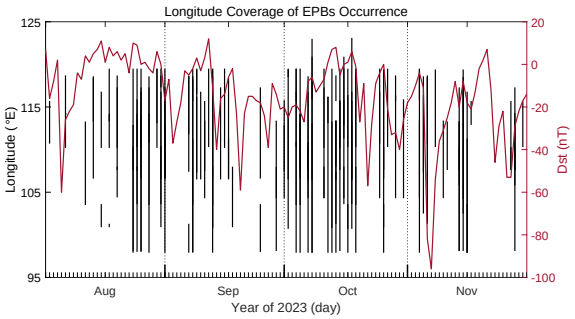

Figure 6. Longitude Coverage of EPBs' Daily Occurrence.

Figure 7 presents daily number of EPB generations for the whole longitudinal observation range. The number tends to increase in August. It is prominently larger in October than in the other months. The number varies randomly under a certain limit in each month.

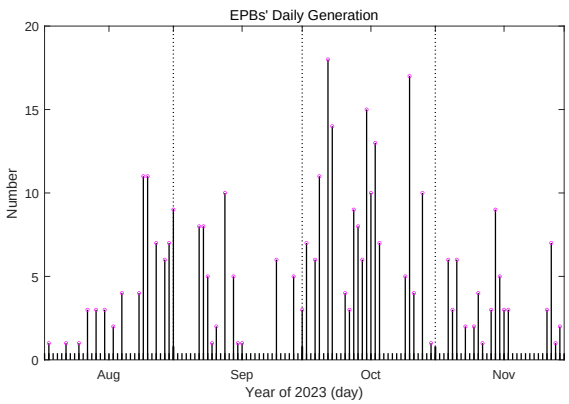

Figure 7. Daily number of EPB generations.

Concerning the longitudinal characteristics of EPBs' generation, since the observation is not evenly distributed in longitudes as shown in Figure 1, we set five longitude belts which are listed in Table 1. We define the monthly generation rate as the ratio of the number of days with EPB generation to the number of days in the specific month. We calculate the monthly generation rate for the five belts separately.

Table 1. Longitude belt division (in °E).

Ln1	Ln2	Ln3	Ln4	Ln5
97.5∼102.5	102.5∼107.5	107.5∼112.5	112.5∼117.5	117.5∼122.5

Figure 8 gives the monthly generation rate for the five belts. In August, the largest one appears at Ln3, although the differences among Ln1, Ln2, and Ln3 are not large. From September to November 2023, the largest generation rate is located at Ln2 of [102.5°E, 107.5°E]. The generation rate decreases almost linearly from Ln2 to Ln5. The generation rates are almost the same in September and November. Note that the generation rates in October are very much higher than the corresponding ones in the other three months.

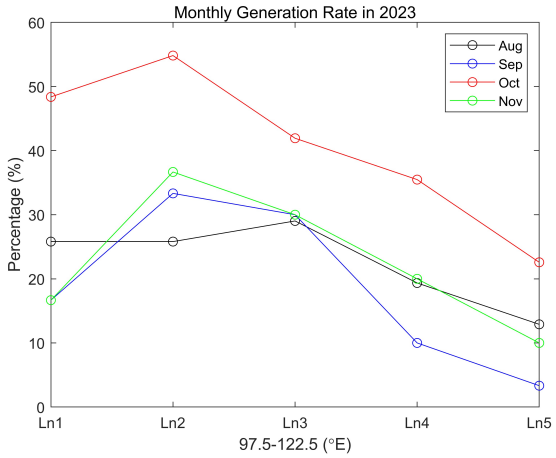

Figure 8. Monthly generation rate of EPBs in 5 belts in the range of [97.5°E, 122.5°E].

4. Discussion

The above results with the dense BDG observation chain reveal various interesting and notable characteristics of the EPBs' generation. The post-sunset EPBs are generally analyzed on their occurrence features. EPBs' generation was previously reported with a few separated GNSS receivers. In this study, we use TFTg of the BDG satellite from longitudinally aligned GNSS receivers which can locate the approximate longitude of the EPBs' generation. The recorded data from August to November enable investigation on the mid-term time variation and statistical characteristics of EPBs' generation.

Figures 3–8 shows that the post-sunset EPBs have a high degree of variability in generation longitude. The quasiperiodic feature of EPBs over the whole longitudinal observation range can be distinguished as one- to multi-scale structures. The generated EPBs generally drift eastward with a speed of ∼110 m/s. For the EPBs generated continuously in time and successively in descending longitude, they catch up and merge with the ones to their east while drifting eastward. The longitude coverage tends to increase from August to the largest value in October and then decrease in November. It is the same as the number of EPBs generated daily and the monthly generation rate.

The generation of EPBs relates with complicated R–T instability [17]. Post sunset is one of the necessary conditions. As the ion production ceases in the E-region, a steep upward density gradient results at F-region bottomside over the magnetic equator. At the same time, a large longitudinal gradient of E-region conductivity arises at the sunset terminator.

To maintain the electric current continuity, the eastward electric field is intensified before the sunset terminator, which is known as the PRE of the eastward electric field [18]. The PRE is one of the most important parameters for R–T instability. The $\overrightarrow{E} \times \overrightarrow{B}$ uplifts the low-density plasma to a higher altitude with a lower recombination rate and ion-neutral collision frequency, which altogether lead to larger growth rate of R-T instability. In addition, if a downward neutral wind exists, the growth rate is enhanced further.

The largest occurrence rate in equinoxes can be related with the geomagnetic declination, when the PRE and hence the upward plasma drift is the largest due to the parallel magnetic field and sunset terminator [11,19]. This can also explain the monthly variations in the longitude coverage and the number of EPB generations in Figures 6 and 7. However, the longitudinal variability of the EPBs' generation in Figures 3–5 cannot be attributed to PRE, which generally has a zonal extent of ∼30°. The generation of the EPBs over a large longitude region could have similar features due to PRE.

The initial perturbation by AGW at the bottomside of the F-region can also be a determinant factor [20]. The generation of EPBs is reported to be preceded by a large-scale wave-like structure (LSWS) of plasma density perturbation [21]. Previous studies showed that an LSWS might be linked with AGW activities [9,22]. Figure 8 clearly shows a wavy pattern of the monthly generation rate over the longitudinal range. The consistent longitudinal distribution suggests a dominant role of an LSWS in the autumn equinox of 2023. It should be pointed out that the scale size of the wave-like structure can be both large and small over a large longitude range, as shown in Figures 3 and 5. The quasiperiodic EPBs with a smaller scale size can cover more than 2500 km in longitude. The scale size of the wave-like structure can be different in different longitudes, as shown in Figure 4, indicating that wave-like structures with different scale sizes can co-exist in the same night.

5. Conclusions

The GION is a newly established GNSS receiver network to make ionospheric observations of the EIA over China. The measurement with signals from GEO satellites of the third generation of the BDS is capable of obtaining the temporal and spatial variations of the ionosphere separately. Defined as the standard deviation of vTEC, a new parameter, TFTg, is proposed to describe the temporal variation of the EPBs. The recorded TFTg in the time–longitude dimension can give the eastward drift speed and display the variation of the EPBs. A mUT-Lon method is proposed to locate the generated longitude of the EPBs.

The post-sunset EPBs observed by the GION from August to November of 2023 have a high degree of variability in their longitudinal characteristics. The longitude of EPBs' generation is generally different on different days. The EPBs over the whole longitudinal observation range can be perceived as one to several structures. If there are three or more structures, they generally show a quasiperiodic feature. The EPBs generally drift eastward with a speed of ∼110 m/s. For those generated continuously in time and successively in descending longitude, the EPBs from west generally catch up with and merge with precedent ones while drifting eastward. The longitude coverage and the number of EPBs generated tend to increase from August to the largest value in October and then decrease in November. The monthly generation rates also have longitudinal variation. They all have a clear wavy pattern and peak over the Ln2 of 102.5–107.5°E from September to November. The monthly generation rate over Ln2 has the largest value in October.

The monthly variation and the statistical behavior of EPBs indicate that the PRE primarily contributes the most from August to November of 2023. The longitudinal variability and the quasiperiodic features of the EPBs' generation can be explained by the LSWS associated with AGW activities. Several processes mostly likely act together to lead the high degree of longitudinal variability of EPBs. Detailed case studies with various kinds of observations, statistical study with a larger dataset, and model work are all needed to clarify the generation of EPBs.

Author Contributions: Conceptualization, G.M.; methodology, G.M., J.L., J.F. and T.M.; software, G.M., J.L. and Q.W.; validation, all authors; data analysis, G.M., J.L., Q.W. and T.M; data curation, all authors; writing—original draft preparation, G.M.; writing—review and editing, G.M., Q.W. and Y.G. All authors have read and agreed to the published version of the manuscript.

Funding: This research was funded by the National Natural Science Foundation of China (Nos. 12073049, 12273062 and 42150105) and the CAS-JSPS Joint Research Project (178GJHZ2023180MI).

Data Availability Statement: The original contributions presented in the study are included in the article, further inquiries can be directed to the corresponding author.

Acknowledgments: We thank all contributors for helping with the GNSS receiver setup for the GION and maintaining the receivers operation. The Dst index was obtained from the GSFC/SPDF OMNIWeb interface at https://omniweb.gsfc.nasa.gov (accessed on 10 March 2024).

Conflicts of Interest: The authors declare no conflicts of interest.

Abbreviations

The following abbreviations are used in this manuscript:

AGW	Atmospheric gravity wave
BDS	BeiDou navigation satellite system
BDG	BDS Geostationary earth orbit
Dst	Disturbance storm-time
EIA	Equatorial ionospheric anomaly
EPB	Equatorial plasma bubble
GAL	Galileo global navigation system of the European Union
GEO	Geostationary earth orbit
GION	GNSS ionospheric observation network
GPS	Global positioning system
GNSS	Global Navigation Satellite System
IPP	Ionospheric pierce point
MIoT	Mobile internet of things
mUT-Lon	Minimum universal time–longitude
NAOC	National Astronomical Observatories of the Chinese Academy of Sciences
PRE	Prereversal enhancement
ROT	rate of TEC change
ROTI	rate of TEC index
R-T	Rayleigh-Taylor
TEC	Total electron content
TFT	Temporal fluctuation of TEC
UT	Universal time

References

1. Albert, J.G.; van Weeren, R.J.; Intema, H.T.; Röttgering, H.J.A. Probabilistic direction-dependent ionospheric calibration for LOFAR-HBA. *A&A* **2020**, *635*, A147.
2. Mangla, S.; Chakraborty, S.; Datta, A.; Paul, A. Exploring Earth's ionosphere and its effect on low radio frequency observation with the uGMRT and the SKA. *J. Astrophys. Astron.* **2023**, *44*, 2. [CrossRef]
3. Rioja, M.; Dodson, R. Subkilometer scale ionospheric studies at the SKA-Low site, using MWA extended baselines. *J. Astron. Telesc. Instrum. Syst.* **2021**, *8*, 011012. [CrossRef]
4. Herscovici-Schiller, O.; Gachet, F.; Couetdic, J.; Meyer, L.; Reynaud, S. A simple ionospheric correction method for radar-based space surveillance systems, with performance assessment on graves data. *Adv. Space Res.* **2023**, *72*, 108–114. [CrossRef]
5. Syndergaard, S.; Kirchengast, G. Systematic ionospheric residual errors in GNSS radio occultation: Theory for spherically stratified media. *Earth Space Sci.* **2022**, *9*, e2022EA002335. [CrossRef]
6. Aragon-Angel, A.; Zürn, M.; Rovira-Garcia, A. Galileo IonosphericCorrection Algorithm: An Optimization Study of NeQuick-G. *Radio Sci.* **2019**, *54*, 1156–1169. [CrossRef]
7. Wang, Y.; Xu, X.H.; Wei, F.S.; Feng, X.S.; Bo, M.H.; Tang, H.W.; Wang, D.S.; Bian, L.; Wang, B.Y.; Zhang, W.Y.; et al. Additional flight delays and magnetospheric–ionospheric disturbances during solar storms. *Sci. Rep.* **2023**, *13*, 3246. [CrossRef]
8. Woodman, R. Spread F—An old equatorial aeronomy problem finally resolved? *Ann. Geophys.* **2009**, *27*, 1915–1934. [CrossRef]

9. Li, G.; Ning, B.; Otsuka, Y.; Abdu, M.A.; Abadi, P.; Liu, Z.; Spogli, L.; Wan, W. Challenges to Equatorial Plasma Bubble and Ionospheric Scintillation Short-Term Forecasting and Future Aspects in East and Southeast Asia. *Surv. Geophys.* **2020**, *42*, 201. [CrossRef]
10. Maruyamam T.; Matuura, N. Longitudinal variability of annual changes in activity of equatorial spread F and plasma bubbles. *J. Geophys. Res.* **1984**, *89*, 10903. [CrossRef]
11. Burke, W.; Gentile, L.; Huang, C.; Valladares, C.; Su, S. Longitudinal variability of equatorial plasma bubbles observed by DMSP and ROCSAT-1. *J. Geophys. Res.* **2004**, *109*, A12301. [CrossRef]
12. Saito, S.; Maruyama, T. Large-scale longitudinal variation in ionospheric height and equatorial spread F occurrences observed by ionosondes. *Geophys. Res. Lett.* **2007**, *34*, L16109. [CrossRef]
13. Li, G.; Otsuka, Y.; Ning, B.; Abdu, M.; Yamamoto, M.; Wan, W.; Liu, L.; Abadi P. Enhanced ionospheric plasma bubble generation in more active ITCZ. *Geophys. Res. Lett.* **2016**, *43*, 2389. [CrossRef]
14. Blewitt, G. An Automatic Editing Algorithm for GPS data. *Geophys. Res. Lett.* **1990**, *17*, 199. [CrossRef]
15. Pi, X.; Mannucci, A.; Lindqwister, U.; Ho, C. Monitoring of global ionospheric irregularities using the Worldwide GPS Network. *Geophys. Res. Lett.* **1997**, *24*, 2283. [CrossRef]
16. Basu, S.; Groves, K.; Quinn, J. Doherty P. A comparison of TEC fluctuations and scintillations at Ascension Island. *J. Atmos. Sol. Terr. Phys.* **1999**, *61*, 1219. [CrossRef]
17. Sultan, P. Linear theory and modeling of the Rayleigh-Taylor instability leading to the occurrence of equatorial spread F. *J. Geophys. Res.* **1996**, *101*, 26875. [CrossRef]
18. Eccles, J.; St Maurice, J.; Schunk, R. Mechanisms underlying the prereversal enhancement of the vertical plasma drift in the low-latitude ionosphere. *J. Geophys. Res. Space Phys.* **2015**, *120*, 4950–4970. [CrossRef]
19. Tsunoda, R. Control of the seasonal and longitudinal occurrence of equatorial scintillations by the longitudinal gradient in integrated E region Pedersen conductivity. *J. Geophys. Res.* **1985**, *90*, 447. [CrossRef]
20. McClure, J.; Singh, S.; Bamgboye, D.; Johnson, F. Kil, H. Occurrence of equatorial F region irregularities: Evidence for tropospheric seeding. *J. Geophys. Res.* **1998**, *103*, 29119. [CrossRef]
21. Tsunoda, R. On the enigma of day-to-day variability in equatorial spread F. *Geophys. Res. Lett.* **2005**, *32*, L08103. [CrossRef]
22. Tsunoda, R. On seeding equatorial spread F: Circular gravity waves, Geophys. *Geophys. Res. Lett.* **2010**, *37*, L10104. [CrossRef]